# Stabilization of a smoothed finite element semi-implicit coupling scheme for viscoelastic fluid–structure interaction

Tao He

*Department of Civil Engineering, Shanghai Normal University, Shanghai 201418, China*

## ARTICLE INFO

## ABSTRACT

We propose in this work a stabilization approach for semi-implicit coupling of viscoelastic fluid–structure interaction (VFSI) using the cell-based smoothed finite element method (CS-FEM). The viscoelastic fluid and nonlinear solid equations are spatially discretized by the CS-FEM and then are semi-implicitly coupled via a partitioned solution strategy. The current semi-implicit coupling framework depends on a second-order characteristic-based split (CBS(B)) scheme that solves the Navier–Stokes equations together with the Oldroyd-B constitutive model in the fractional-step manner. To enhance the stability of the semi-implicit coupling algorithm, the discrete elastic-viscous split stress-gradient (DEVSS-G) procedure is introduced into the explicit stage while the stabilized pressure gradient projection (SPGP) is earmarked for the implicit stage. Moreover, the iterated end-of-step velocity begins with the intermediate velocity during the subiterations. The DEVSS-G/CBS(B)-SPGP technique is readily applied to the CBS-based partitioned semi-implicit coupling algorithm for VFSI. Visible improvements in stabilization and efficiency are revealed in a benchmark test.

## 1. Introduction

Viscoelastic fluid–structure interaction (VFSI), which generally characterizes the mutual interplay between viscoelastic fluid flows and rigid/flexible bodies [1,2], frequently takes place in a rich variety of biological and industrial systems. Two common VFSI examples are, respectively, the blood transportation through human cardiovascular system and the crude oil flow inside an oscillating cylindrical marine riser. In VFSI, the viscoelastic fluid flow exhibits complex rheological properties that complicate the responses of the wetted structures accordingly. Especially, the flow velocity, pressure and viscoelastic stress undergo significant fluctuations near the fluid–structure interfaces in response to the time-varying geometry caused by large structural displacement and/or finite solid deformation. Furthermore, the hyperbolic constitutive equation probably poses major numerical difficulties in describing exact flow phenomena of a viscoelastic fluid in principle since the viscoelastic stress tensor arises as a third variable that evolves in time and is tightly coupled with the velocity and pressure fields [3]. Therefore, simulating VFSI has been identified as a more challenging task than Newtonian FSI (NFSI) modeling. Given the realistic importance, computational scientists have shown continuing interests in developing stable, efficient and robust numerical methods for VFSI in this century.

Till now, many research papers have been dedicated to accurate prediction of VFSI and its resultant multi-physical phenomena.

Chakraborty et al. [4,5] calculated steady viscoelastic fluid flows in a two-dimensional collapsible channel using the finite element method (FEM) [6]. Three constitutive models are taken into consideration in the fluid component. An elastic segment of the upper wall of the channel is modeled as a zero-thickness membrane by introducing a force term into the fluidic momentum equation. The set of simultaneous viscoelastic equations is treated via a discrete elastic-viscous stress split-traceless gradient (DEVSS-TG) formulation and is further stabilized by the streamline upwind/Petrov–Galerkin method [7]. The steady viscoelastic flow of a two-dimensional collapsible channel containing a deformable finite-thickness elastic wall was subsequently analyzed in [8] using the same mixed FEM. The coupled equations are simultaneously linearized in a monolithic system without the inertial force of fluid and solid media. It is noticed in [4,5,8] that the fluid governing equations need not be computed on a moving finite element mesh since the creeping flow is very slow. Chen et al. [9] employed the standard partitioned implicit coupling algorithm under the arbitrary Lagrangian–Eulerian (ALE) description [10] to calculate an Oldroyd-B fluid [11] interacting with an elastic solid. To that end, fixed-point method accelerated by Aitken's $\Delta^2$ method [12] is performed to strongly couple individual fields through different software packages and interface library. A mass–spring–dashpot model [13] is also extended to qualitatively study the dynamic behavior of VFSI considering different physical parameters. Amini et al. [14] adopted a commercial FE

software to study the yield stress and shear-thinning behaviors of a Herschel–Bulkley fluid flow. The fluid–structure coupling is likewise realized under creeping flow conditions, though the Mooney–Rivlin hyperelastic model is used to account for finite deformation. In a conference paper [15], a partitioned semi-implicit coupling method [16] is applied to simulate the open cavity flow of an Oldroyd-B fluid interacting with the flexible thick bottom. The structure is simplified as an Euler–Bernoulli beam in the preliminary VFSI study. It appears that periodic oscillations of the bottom are underestimated in comparison with other results [2,9]. It is likely to attribute this outcome to the thicker but lighter solid model. Lee and Xu [17] utilized partitioned and monolithic solution algorithms for simulating a hemodynamic VFSI problem, respectively. In both approaches, the structure is mathematically described by an isotropic linear elastic model which simply experiences small deformation. Later, viscoelastic fluid flow past a flexibly mounted circular cylinder was investigated in [18] to understand the underlying vortex-induced vibration mechanism at different Reynolds numbers. For this purpose, an ALE finite volume formulation is applied to the FENE-P fluid flow computation whereas the rigid cylinder is allowed to vibrate transversely only. A partitioned explicit coupling scheme is responsible for the loose coupling of viscoelastic fluid flow and rigid-body motion therein. Zhu [19] conducted an immersed-boundary analysis of three-dimensional interaction between highly flexible solids and Oldroyd-B/FENE-P fluids. The viscoelastic fluids are specially modeled by the lattice Boltzmann method in the Eulerian reference so that large mesh deformation can be avoided. Most recently, He [2] proposed a strongly-coupled VFSI solver based on the cell-based smoothed finite element method (CS-FEM) [20]. The incompressible flow of an Oldroyd-B fluid and finite deformation of an elastic solid are tightly coupled within the ALE framework. The spatial discretization of the two physical media is accomplished with the CS-FEM that smooths all gradient related terms of field equations. Two transient VFSI benchmark problems are then settled in consideration of inertial effect [2].

In addition, a few efforts have been made to moving-boundary viscoelastic flow problems such as free surface flows [21], moving boundary–initial value problems [22] and forced motions [23]. The ALE method is still adopted in all these papers mainly because of its conceptual and operational simplicity.

In view of drastic nonlinearities of physically distinct interacting fields, partitioned procedures are normally favored to address the coupled mechanical analyses of multi-physical systems [24]. Strategically speaking, heterogeneous disciplines are sequentially solved such that the utilization and management of available code resources demand minimal modifications. As for FSI, the widespread computing methods involve partitioned explicit and implicit coupling algorithms under the ALE description [12,25–27]. In theory, the former is computational inexpensive whereas the latter is physically conservative. They are absolutely applicable to VFSI, as reviewed above.

Apart from the explicit and implicit partitioned methods, a third partitioned solution method, called the projection-based partitioned semi-implicit coupling algorithm [16], has been proposed in terms of the classic Chorin–Témam projection [28,29] for simulating hemodynamic NFSI problems. The terminology "semi-implicit" emanates from an explicit–implicit or partially-implicit treatment that consists of two major steps in charge of the underlying multi-physical coupling. Firstly, the domain mesh is intentionally extrapolated where the fluid computation covers the ALE-advection–diffusion phase only. Secondly, the corrected velocity and updated pressure of the fluid are iterated with the structural movement on the temporarily fixed mesh. In contrast to the fully implicit coupling scheme, the semi-implicit coupling scheme enables reduced overheads of updating dynamic mesh without too much stability loss [16]. Nowadays intriguing variants of the semi-implicit coupling algorithm have been developed for NFSI, see [30–33] for reference.

On account of the pioneering work of Fernández et al. [16] and the characteristic-based split (CBS) scheme presented by Zienkiewicz et al. [34], the author has devised the CBS-based partitioned semi-implicit coupling scheme for fluid–rigid/flexible body interaction [35]. It is noted that a high-order convective stabilization term derived from the characteristic-Galerkin procedure is naturally implanted into the partitioned semi-implicit coupling algorithm. As a result, the CBS-based partitioned semi-implicit coupling algorithm can inherit the stabilization effect from the CBS fluid solver and the computing economy from its projection-based counterpart. He et al. [36] later designed two improved CBS-based partitioned semi-implicit coupling algorithms integrating Split A and Split B [37]. The two easy-to-implement schemes are named the CBS(A)-based and CBS(B)-based partitioned semi-implicit coupling methods where the end-of-step velocity is iterated at the implicit stage. Extremely low mass ratios are achieved in laminar region, provided that the stabilized pressure gradient projection (SPGP) [38,39] is used for the second-order pressure accurate CBS(B) scheme. Such a treatment underpins the stabilized CBS(B)-based partitioned semi-implicit coupling algorithm we prepare for VFSI here.

Unfortunately, few applications of the partitioned semi-implicit coupling method have yet emerged to cater for VFSI, except [15,40]. The main impetus of the present study is to expand the CBS-based partitioned semi-implicit coupling algorithm towards VFSI with demonstrated computational benefits. However, the contrived semi-implicit decoupling appears non-physical among cut modules, possibly incurring improper communications of the triple fluid variables and structural responses through the interface. Further to the constitutive model, the Oldroyd-B fluid seems simple but retains extravagant extensional and constant shear viscosities that still render certain unwanted difficulties [3]. These numerical dilemmas have necessitated special stabilization of the CBS-based semi-implicit coupling algorithm for stable numerical approximation. In what follows, the SPGP technique [38], which aims to stabilize the second-order splitting error in pressure for the projection method [28,29], contributes to the DEVSS-G formulation of viscoelastic fluid equations being semi-implicitly decoupled in the ALE context. Here, both the viscoelastic fluid and nonlinear solid are spatially discretized by the CS-FEM [41] since the standard FEM overestimates the stiffness matrix of the discrete model related to the fully compatible strain field [6]. The inherent capacity for severe mesh deformation [42,43] and economical time consumption [44] continues to show signs of the method's advantages. These properties possibly make the CS-FEM become a competitive candidate for computational VFSI simulation.

The remainder of this paper is outlined as follows. The principle of the CS-FEM is briefly discussed in Section 2. Section 3 focuses on the incompressible viscoelastic fluid flow whereas Section 4 explains the structural dynamics of an elastic solid subjected to the viscoelastic fluid force. The mesh deformation method is then articulated in Section 5. Section 6 interprets the proposed partitioned semi-implicit coupling algorithm step by step. A benchmark example is tackled in Section 7, followed by the conclusions drawn in Section 8.

## 2. Fundamentals of CS-FEM

### 2.1. Cell-based gradient smoothing

Let $\widetilde{\Omega}$ be a two-dimensional, continuous and bounded SC, and $\widetilde{\Gamma}$ the smooth boundary of $\widetilde{\Omega}$. We define, for simplicity, a scalar-valued function $f$ at a point $\mathbf{x}_c$ in $\widetilde{\Omega}$. The model diagram is depicted in Fig. 1 where $O$, $x_1$ and $x_2$ denote the origin, horizontal and vertical axes of the Cartesian coordinate system, respectively. In the SC, the smoothed gradient of $f$ at the point of interest may be structured below [20]

$$\widetilde{\nabla} f(\mathbf{x}_c) = \int_{\widetilde{\Omega}} \nabla f(\mathbf{x}) W(\mathbf{x} - \mathbf{x}_c) \, d\Omega, \quad \forall \, \mathbf{x}_c \in \widetilde{\Omega}, \tag{1}$$
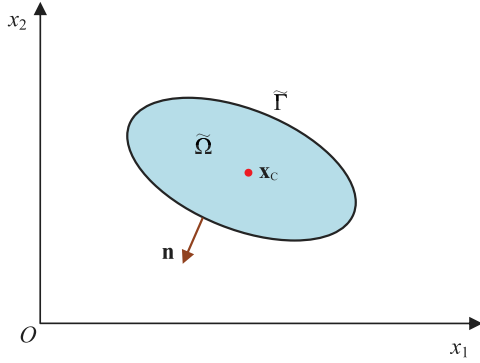
Fig. 1. Cell-based gradient smoothing in a generic SC.



Fig. 2. Configuration of SCs and shape functions for $n_c = 4$.

where $\nabla$ and $\widetilde{\nabla}$ represents the gradient operator and its smoothed counterpart, respectively, $\mathbf{x}$ denotes the spatial coordinates and $W$ is the smoothing kernel. Suppose that $W$ meets the positivity and unity requirements [45]

$$W(\mathbf{x} - \mathbf{x}_c) \geqslant 0 \quad \text{and} \quad \int_{\widetilde{\Omega}} W(\mathbf{x} - \mathbf{x}_c) \, d\Omega = 1. \tag{2}$$

We may consider $W$ as a Heaviside-type step function [20,46]

$$W(\mathbf{x} - \mathbf{x}_c) = \begin{cases} \dfrac{1}{A_c}, & \mathbf{x} \in \widetilde{\Omega}, \\ 0, & \mathbf{x} \notin \widetilde{\Omega}, \end{cases} \tag{3}$$

where $A_c$ is the area of $\widetilde{\Omega}$.

After applying integration by parts into the right-hand side of Eq. (1), we can get

$$\widetilde{\nabla} f(\mathbf{x}_c) = \int_{\widetilde{\Gamma}} f(\mathbf{x}) \mathbf{n}(\mathbf{x}) W(\mathbf{x} - \mathbf{x}_c) \, d\Gamma - \int_{\widetilde{\Omega}} f(\mathbf{x}) \nabla W(\mathbf{x} - \mathbf{x}_c) \, d\Omega, \tag{4}$$

where $\mathbf{n}$ signifies the unit outward normal to $\widetilde{\Gamma}$ (refer to Fig. 1). Substituting Eq. (3) into Eq. (4) then yields

$$\widetilde{\nabla} f(\mathbf{x}_c) = \frac{1}{A_c} \int_{\widetilde{\Gamma}} f(\mathbf{x}) \mathbf{n}(\mathbf{x}) \, d\Gamma, \tag{5}$$

where the gradient of the constant kernel has vanished of itself. Eq. (5) is readily transformed into its algebraic form

$$\widetilde{\nabla} f(\mathbf{x}_c) = \frac{1}{A_c} \sum_{i=1}^{n_1} f(\mathbf{x}_i^{\text{mp}}) \mathbf{n}(\mathbf{x}_i^{\text{mp}}) l_i, \tag{6}$$

where $n_1$ means the number of segments that compose $\widetilde{\Gamma}$, $\mathbf{x}_i^{\text{mp}}$ represents the spatial coordinates of the midpoint on the $i$th segment $\widetilde{\Gamma}_i$ and $l_i$ is the length of $\widetilde{\Gamma}_i$. Eq. (5) or Eq. (6) indicates that the cell-based smoothed gradient is definitely irrelevant to the location of integration point inside the SC [42]. For this reason, the CS-FEM possesses an inherent flexibility of integrating the smoothed Galerkin weak form of partial differential equations dominating a vast majority of physical laws [42,44].

### 2.2. Cell-by-cell integration

For spatial discretization, a computational domain $\Omega$ is discretized into $n_e$ Q4 elements as usual. That is to say, $\Omega = \overline{\Omega}_1 \cup \overline{\Omega}_2 \cup \cdots \cup \overline{\Omega}_{n_e}$ and $\overline{\Omega}_i \cap \overline{\Omega}_j = \varnothing$ where $1 \leqslant i, j \leqslant n_e$ and $i \neq j$. Each Q4 element is further subdivided into a number of complementary SCs such that $\overline{\Omega}_i = \widetilde{\Omega}_{i1} \cup \widetilde{\Omega}_{i2} \cup \cdots \cup \widetilde{\Omega}_{in_c}$ where $n_c$ is the number of the SCs forming the $i$th element. After that, the integration rule of the CS-FEM is explicitly explicated on a cell-by-cell basis

$$\int_{\Omega} f(\mathbf{x}) \, d\Omega = \sum_{i=1}^{n_e} \int_{\overline{\Omega}_i} f(\mathbf{x}_i) \, d\Omega = \sum_{i=1}^{n_e} \sum_{j=1}^{n_c} \int_{\widetilde{\Omega}_{ij}} f(\mathbf{x}_{ij}) \, d\Omega$$
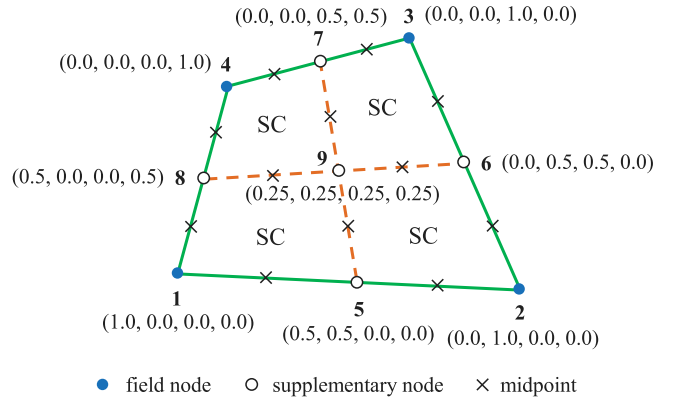
$$= \sum_{i=1}^{n_e} \sum_{j=1}^{n_c} f(\mathbf{x}_{ij}) A_{cij}, \quad \mathbf{x}_{ij} \in \widetilde{\Omega}_{ij}, \tag{7}$$

which indicates that the CS-FEM avoids the traditional isoparametric mapping and maintains certain mesh-free properties in association with the gradient smoothing.

### 2.3. SC configuration and shape functions

A wide range of possibilities that we deploy SCs in a Q4 element can be explored as long as the arrangement satisfies the stability condition. In each element, the minimum SCs have to be considered to guarantee the order of the smoothed Galerkin weak form integral [47]. Specifically, $n_c \geqslant 2$ is able to meet that stability constraint as is proved in the textbook [47]. In most situations, $n_c = 4$ is advocated for the sake of a good balance between the stability and efficiency [20,48]. Fig. 2 illuminates the common SC partition of $n_c = 4$. We are aware that the augmented shape functions at five virtual nodes are simply calculated by averaging the values at four corners. Hence additional degrees of freedom are never added to the final discrete model. The centroid of the Q4 element (i.e., Node 9 in Fig. 2) is recommended here as the optimal integration point [42]. The essential properties of the configured shape functions are not repeated here since they are detailed in [47].

## 3. Viscoelastic fluid flow with moving boundaries

### 3.1. Governing equations

The unsteady isothermal, laminar flow of an incompressible viscoelastic fluid occupying a moving domain $\Omega_f \subset \mathbb{R}^2$ in a time interval $(0, t_\infty)$ is governed by the mass and momentum conservations under the ALE description

$$\nabla \cdot \mathbf{u} = 0 \quad \text{on} \quad \Omega_f \times (0, t_\infty), \tag{8}$$

$$\rho_f \left( \left. \frac{\partial \mathbf{u}}{\partial t} \right|_{\mathbf{x}_0} + \mathbf{w} \cdot \nabla \mathbf{u} - \mathbf{g}_f \right) - \nabla \cdot \boldsymbol{\sigma}_f = \mathbf{0} \quad \text{on} \quad \Omega_f \times (0, t_\infty), \tag{9}$$

where $\left. \frac{\partial(\cdot)}{\partial t} \right|_{\mathbf{x}_0}$ is the time derivative in the ALE notation, $\mathbf{x}_0$ the position of the fixed reference configuration, $\rho_f$ the fluid density, $\mathbf{u}$ the flow velocity, $\mathbf{w} = \mathbf{u} - \mathbf{u}_m$ the ALE convective velocity, $\mathbf{u}_m$ the mesh velocity, $\mathbf{g}_f$ the body acceleration of the fluid, $\boldsymbol{\sigma}_f$ the Cauchy stress and $t$ the time. The Cauchy stress of the viscoelastic fluid can be written as

$$\boldsymbol{\sigma}_f = -p\mathbf{I} + \mathbb{T}, \tag{10}$$

where $p$ is the pressure, $\mathbf{I}$ the identity tensor and $\mathbb{T}$ the extra stress. Generally, the extra stress is decomposed into solvent and polymeric contributions

$$\mathbb{T} = 2\mu_s \epsilon + \tau \quad \text{and} \quad \epsilon = \frac{1}{2} \left( \nabla \mathbf{u} + (\nabla \mathbf{u})^{\text{T}} \right), \tag{11}$$

where $\mu_s$ is the solvent viscosity, $\epsilon$ means the deformation rate tensor, superscript T denotes transpose and $\tau$ signifies the viscoelastic stress. The constitutive equation of the Oldroyd-B fluid model [11] reads

$$\tau + \lambda \overset{\triangledown}{\tau} = 2\mu_p \epsilon, \tag{12}$$

where $\lambda$ represents the relaxation time, $\triangledown$ denotes the upper-convected time derivative and $\mu_p$ is the polymer viscosity. In the ALE context, $\overset{\triangledown}{\tau}$ is explicitly expressed as

$$\overset{\triangledown}{\tau} = \frac{\partial \tau}{\partial t}\Big|_{\mathbf{x}_0} + \mathbf{w} \cdot \nabla \tau - \left( (\nabla \mathbf{u})^{\mathrm{T}} \cdot \tau + \tau \cdot \nabla \mathbf{u} \right). \tag{13}$$

To strengthen the positive definite property of Eq. (12), the polymeric contribution may be reformulated below

$$\tau = \frac{\mu_p}{\lambda}(\mathbf{c} - \mathbf{I}), \tag{14}$$

in the light of the conformation tensor $\mathbf{c}$ [49]. With this relationship in hand, the constitutive law of the Oldroyd-B fluid admits the following representation

$$\frac{\partial \mathbf{c}}{\partial t}\Big|_{\mathbf{x}_0} + \mathbf{w} \cdot \nabla \mathbf{c} - \left( (\nabla \mathbf{u})^{\mathrm{T}} \cdot \mathbf{c} + \mathbf{c} \cdot \nabla \mathbf{u} \right) + \frac{1}{\lambda}(\mathbf{c} - \mathbf{I}) = \mathbf{0}, \tag{15}$$

whereby the corresponding viscoelastic fluid equations are well-posed in a mathematical sense.

To simplify the fluid computation, we define the following dimensionless scales

$$\mathbf{x}^* = \frac{\mathbf{x}}{L}, \ t^* = \frac{tU}{L}, \ \mathbf{u}^* = \frac{\mathbf{u}}{U}, \ \mathbf{w}^* = \frac{\mathbf{w}}{U}, \ p^* = \frac{p}{\rho_f U^2}, \ \mathbf{c}^* = \mathbf{c}, \ \mathbf{I}^* = \frac{\mathbf{I}U}{L}, \ \mathbf{g}_f^* = \frac{\mathbf{g}_f L}{U^2},$$

on grounds of the free-stream velocity $U$ and the characteristic length $L$. Applying these scales and dropping all asterisks afterwards, the dimensionless version of the governing equations is finalized as

$$\nabla \cdot \mathbf{u} = 0, \tag{16}$$

$$\frac{\partial \mathbf{u}}{\partial t}\Big|_{\mathbf{x}_0} + \mathbf{w} \cdot \nabla \mathbf{u} + \nabla p - \frac{\eta}{Re}\nabla^2 \mathbf{u} - \frac{1-\eta}{ReWi}\nabla \cdot \mathbf{c} - \mathbf{g}_f = \mathbf{0}, \tag{17}$$

$$\overset{\triangledown}{\mathbf{c}} + \frac{1}{Wi}(\mathbf{c} - \mathbf{I}) = \mathbf{0}, \tag{18}$$

where $\eta = \frac{\mu_s}{\mu}$ is the viscosity ratio, $\mu = \mu_s + \mu_p$ the total shear viscosity, $Re = \frac{\rho_f U L}{\mu}$ the Reynolds number and $Wi = \frac{\lambda U}{L}$ the Weissenberg number. Furthermore, appropriate boundary and initial conditions are needed to close the set of viscoelastic fluid equations.

### 3.2. DEVSS-G/CBS(B)-SPGP algorithm

It is found that the DEVSS-G method introduces an elliptic operator to stabilize the discrete viscoelastic momentum equation and also discards the objective derivative of the deformation rate tensor [50]. More importantly, this technique is applicable to any class of constitutive equations [50]. It is thus quite natural to ally the DEVSS-G method with the conformation tensor. For this reason, we may recast Eq. (17) into

$$\frac{\partial \mathbf{u}}{\partial t}\Big|_{\mathbf{x}_0} + \mathbf{w} \cdot \nabla \mathbf{u} - \mathbf{g}_f = -\nabla p + \frac{\eta+\theta}{Re}\nabla^2 \mathbf{u} - \frac{\theta}{Re}\nabla \cdot \mathbb{G} + \frac{1-\eta}{ReWi}\nabla \cdot \mathbf{c}, \tag{19}$$

where $\mathbb{G} = \nabla \mathbf{u}$ is the $L^2$-projection of the velocity gradient [51] and $\theta = 1 - \eta$ the stabilization parameter. Obviously, the elliptic operator will vanish in a transparent way if the exact solution to Eq. (19) is recovered. The added cost and complexity in weak form are marginal in comparison with the DEVSS method [52].

On the other hand, the second-order CBS(B) scheme is found not very stable especially for steady-state Newtonian flows because of the pressure difference [39]. The reduced pressure stabilization is of course the penalty of increasing the order of splitting error in pressure. To settle this formidable issue, Nithiarasu and Zienkiewicz [39] turned to the SPGP technique [38] for assistance. Similarly, care must be taken to rule out any possibility that the CBS(B) scheme becomes unstable in creeping viscoelastic flows.

To apply the SPGP technique, an auxiliary equation is first defined

$$\mathbf{q} - \nabla p = \mathbf{0}, \tag{20}$$

where $\mathbf{q}$ is the auxiliary variable. Using Eq. (20), we can modify Eq. (16) as

$$\nabla \cdot \mathbf{u} + \phi \nabla \cdot \mathbf{q} - \phi \nabla^2 p = 0, \tag{21}$$

where $\phi$ denotes the stabilization parameter being discussed elsewhere [53,54].

Then Eqs. (21), (19) and (20) are discretized in time as follows

$$\nabla \cdot \mathbf{u}^{n+1} + \phi \nabla \cdot \mathbf{q}^n - \phi \nabla^2 p^{n+1} = 0, \tag{22}$$

$$\frac{\mathbf{u}^{n+1} - \mathbf{u}^n}{\Delta t} = -\mathbf{w}^n \cdot \nabla \mathbf{u}^n - \nabla p^{n+1} + \nabla p^n - \nabla p^n$$
$$+ \frac{\eta+\theta}{Re}\nabla^2 \mathbf{u}^n - \frac{\theta}{Re}\nabla \cdot \mathbb{G}^n + \frac{1-\eta}{ReWi}\nabla \cdot \mathbf{c}^n + \mathbf{g}_f^n, \tag{23}$$

$$\mathbf{q}^{n+1} - \nabla p^{n+1} = \mathbf{0}, \tag{24}$$

where $\mathbf{q}$ is explicitly treated and $p$ is implicitly advanced. To go further, Eq. (23) is divided into two parts

$$\frac{\mathbf{v} - \mathbf{u}^n}{\Delta t} = -\mathbf{w}^n \cdot \nabla \mathbf{u}^n - \nabla p^n + \frac{\eta+\theta}{Re}\nabla^2 \mathbf{u}^n - \frac{\theta}{Re}\nabla \cdot \mathbb{G}^n + \frac{1-\eta}{ReWi}\nabla \cdot \mathbf{c}^n + \mathbf{g}_f^n, \tag{25}$$

$$\frac{\mathbf{u}^{n+1} - \mathbf{v}}{\Delta t} = -\nabla(p^{n+1} - p^n), \tag{26}$$

where $\mathbf{v}$ indicates the intermediate velocity and the pressure gradient term is kept in line with Split B [37].

Following the CBS procedure [34], the main steps of the proposed DEVSS-G/CBS(B)-SPGP algorithm are interpreted below

Step 1: Predict the velocity

$$\frac{\mathbf{v} - \mathbf{u}^n}{\Delta t} = -\mathbf{w}^n \cdot \nabla \mathbf{u}^n - \nabla p^n + \frac{\eta+\theta}{Re}\nabla^2 \mathbf{u}^n - \frac{\theta}{Re}\nabla \cdot \mathbb{G}^n + \frac{1-\eta}{ReWi}\nabla \cdot \mathbf{c}^n$$
$$+ \frac{\Delta t}{2}\mathbf{w}^n \cdot \nabla \left( \mathbf{w}^n \cdot \nabla \mathbf{u}^n + \nabla p^n + \frac{\theta}{Re}\nabla \cdot \mathbb{G}^n - \frac{1-\eta}{ReWi}\nabla \cdot \mathbf{c}^n \right), \tag{27}$$

Step 2: Update the pressure

$$\nabla^2 p^{n+1} = \frac{1}{\Delta t + \phi}\left( \nabla \cdot \mathbf{v} + \Delta t \nabla^2 p^n + \phi \nabla \cdot \mathbf{q}^n \right), \tag{28}$$

Step 3: Correct the velocity

$$\frac{\mathbf{u}^{n+1} - \mathbf{v}}{\Delta t} = -\nabla(p^{n+1} - p^n) + \frac{\Delta t}{2}\mathbf{w}^n \cdot \nabla^2(p^{n+1} - p^n), \tag{29}$$

Step 4: Renew the velocity and pressure gradients

$$\mathbb{G}^{n+1} = \nabla \mathbf{u}^{n+1} \quad \text{and} \quad \mathbf{q}^{n+1} = \nabla p^{n+1}, \tag{30}$$

Step 5: Calculate the conformation tensor

$$\frac{\mathbf{c}^{n+1} - \mathbf{c}^n}{\Delta t} = -\mathbf{w}^n \cdot \nabla \mathbf{c}^n + \left( (\nabla \mathbf{u})^{\mathrm{T}} \cdot \mathbf{c} + \mathbf{c} \cdot \nabla \mathbf{u} \right)^n - \frac{1}{Wi}(\mathbf{c}^n - \mathbf{I})$$
$$+ \frac{\Delta t}{2}\mathbf{w}^n \cdot \nabla \left( \mathbf{w}^n \cdot \nabla \mathbf{c}^n - \left( (\nabla \mathbf{u})^{\mathrm{T}} \cdot \mathbf{c} + \mathbf{c} \cdot \nabla \mathbf{u} \right)^n + \frac{1}{Wi}(\mathbf{c}^n - \mathbf{I}) \right), \tag{31}$$

where $\Delta t = t^{n+1} - t^n$ denotes the time step, and the body force and third-order terms are neglected.

It is of interest to remark that the semi-implicit CBS(B) scheme is also conditionally stable [37,55]. For the viscoelastic flow, the general time-step limitations are recommended below

$$\Delta t \leqslant \Delta t_{crit} = \min(\Delta t_{conv}, \ \Delta t_{diff}, \ \Delta t_{visc}), \tag{32}$$

where $\Delta t_{crit}$ is the critical time step, and $\Delta t_{conv}$, $\Delta t_{diff}$ and $\Delta t_{visc}$ represent, respectively, the convection, diffusion and viscoelasticity limits calculated from

$$\Delta t_{conv} = \frac{h}{|\mathbf{u}|}, \quad \Delta t_{diff} = \frac{1}{2}h^2 Re, \quad \Delta t_{visc} = h\sqrt{ReWi}, \tag{33}$$

where $h$ signifies the characteristic length of a local element.

Concerning the pressure stabilization parameter, the following inequality should be satisfied

$$\phi \leqslant \frac{1}{4} h^2 Re, \tag{34}$$

in the interest of the numerical stability and computational convergence [38]. According to [36,54], the constraint on $\phi$ can be safely replaced with

$$\phi \leqslant \min(0.5 \Delta t_{\text{crit}}, \ 1.0 \Delta t). \tag{35}$$

To make Eq. (35) hold, $\phi = 0.25\Delta t$ is generally advocated in previous studies [38,39,53]. For the CS-FEM, He et al. [54] numerically investigated the effect of $\phi$ on steady-state cavity flow of a Newtonian fluid. Since $\phi = 0.1\Delta t$ works slightly better therein, such a choice is employed for the current scenario.

### 3.3. Spatial discretization for the fluid

The standard Galerkin procedure is applied to discretize the fluid equations in space. The primitive and auxiliary variables can be approximated using equal linear interpolations. In association with the CS-FEM, the fully discrete form of the DEVSS-G/CBS(B)-SPGP scheme is written as follow

$$\mathbf{M}_{\text{f}}(\bar{\mathbf{v}} - \bar{\mathbf{u}}^n) = -\Delta t \left( \widetilde{\mathbf{C}}_{\text{u}}^n \bar{\mathbf{u}}^n + \widetilde{\mathbf{G}} \bar{\mathbf{p}}^n + \frac{\eta + \theta}{Re} \widetilde{\mathbf{H}} \bar{\mathbf{u}}^n + \frac{\theta}{Re} \widetilde{\mathbf{G}} \bar{\mathbb{G}}^n - \frac{1-\eta}{ReWi} \widetilde{\mathbf{G}} \bar{\mathbf{b}}^n \right)$$
$$- \frac{(\Delta t)^2}{2} \left( \widetilde{\mathbf{K}}_{\text{u}}^n \bar{\mathbf{u}}^n + \widetilde{\mathbf{Q}}^n \bar{\mathbf{p}}^n + \frac{\theta}{Re} \widetilde{\mathbf{Q}}^n \bar{\mathbb{G}}^n - \frac{1-\eta}{ReWi} \widetilde{\mathbf{Q}}^n \bar{\mathbf{b}}^n \right), \tag{36}$$

$$\widetilde{\mathbf{H}} \bar{\mathbf{p}}^{n+1} = -\frac{1}{\Delta t + \phi} \left( \widetilde{\mathbf{G}} \bar{\mathbf{v}} - \Delta t \widetilde{\mathbf{H}} \bar{\mathbf{p}}^n + \phi \widetilde{\mathbf{G}} \bar{\mathbf{q}}^n \right), \tag{37}$$

$$\mathbf{M}_{\text{f}}(\bar{\mathbf{u}}^{n+1} - \bar{\mathbf{v}}) = -\Delta t \left( \widetilde{\mathbf{G}}(\bar{\mathbf{p}}^{n+1} - \bar{\mathbf{p}}^n) + \frac{\Delta t}{2} \widetilde{\mathbf{Q}}^n(\bar{\mathbf{p}}^{n+1} - \bar{\mathbf{p}}^n) \right), \tag{38}$$

$$\mathbf{M}_{\text{f}} \bar{\mathbb{G}}^{n+1} = \widetilde{\mathbf{G}} \bar{\mathbf{u}}^{n+1} \quad \text{and} \quad \mathbf{M}_{\text{f}} \bar{\mathbf{q}}^{n+1} = \widetilde{\mathbf{G}} \bar{\mathbf{p}}^{n+1}, \tag{39}$$

$$\mathbf{M}_{\text{f}}(\bar{\mathbf{c}}^{n+1} - \bar{\mathbf{c}}^n) = -\Delta t \left( \widetilde{\mathbf{C}}_{\text{u}}^n \bar{\mathbf{c}}^n - \widetilde{\mathbf{D}}_{\text{c}}^n \bar{\mathbf{c}}^n + \frac{1}{Wi}(\mathbf{M}_{\text{f}} \bar{\mathbf{c}}^n - \mathbf{I}) \right.$$
$$\left. + \frac{\Delta t}{2} \left( \widetilde{\mathbf{K}}_{\text{u}}^n \bar{\mathbf{c}}^n - \widetilde{\mathbf{E}}_{\text{c}}^n \bar{\mathbf{c}}^n + \frac{1}{Wi}(\widetilde{\mathbf{L}}^n \bar{\mathbf{c}}^n - \mathbf{I}) \right) \right), \tag{40}$$

where the bar indicates a nodal quantity and the assembled coefficient matrices can be found in [2].

## 4. Finite solid deformation

### 4.1. Governing equations

Consider that a two-dimensional elastic solid seizes a smooth, continuous and bounded physical domain $\Omega_{\text{s}} \subset \mathbb{R}^2$. The flexible body is constantly subject to the fluctuating fluid forces as a result of prolonged exposure to the incident viscoelastic flow. The elastodynamics equation stating the conservation law of momentum of the solid continuum may be expressed in the absence of structural damping

$$\rho_{\text{s}} \left( \ddot{\mathbf{d}} - \mathbf{g}_{\text{s}} \right) - \nabla \cdot \boldsymbol{\sigma}_{\text{s}} = \mathbf{0} \quad \text{on} \quad \Omega_{\text{s}} \times (0, \ t_\infty), \tag{41}$$

where the dot means the derivative with respect to $t$, $\rho_{\text{s}}$ is the structural density, $\mathbf{g}_{\text{s}}$ indicates the body acceleration of the solid and $\boldsymbol{\sigma}_{\text{s}}$ is the solid Cauchy stress. For the geometrically nonlinear analysis, the Saint Venant–Kirchhoff constitutive model is assumed

$$\mathbf{S} = \mathbf{D} : \mathbf{E} \quad \text{and} \quad \mathbf{E} = \frac{1}{2}(\mathbf{F}^{\text{T}}\mathbf{F} - \mathbf{I}), \tag{42}$$

where $\mathbf{S}$ signifies the second Piola–Kirchhoff stress, $\mathbf{E}$ denotes the Green–Lagrange strain, $\mathbf{F} = \mathbf{I} + \nabla \mathbf{d}$ means the deformation gradient and $\mathbf{D}$ is the elastic constitutive matrix associated with Young's modulus $E$

and Poisson's ratio $\nu$ on the plane stress assumption. We may transfer $\mathbf{S}$ to $\boldsymbol{\sigma}_{\text{s}}$ through the geometric transformation

$$\boldsymbol{\sigma}_{\text{s}} = \frac{1}{J} \mathbf{F} \mathbf{S} \mathbf{F}^{\text{T}}, \tag{43}$$

where $J = \det(\mathbf{F})$ is the Jacobian.

Similarly, the following dimensionless scales

$$\mathbf{x}^* = \frac{\mathbf{x}}{L}, \ t^* = \frac{tU}{L}, \ \mathbf{d}^* = \frac{\mathbf{d}}{L}, \ E^* = \frac{E}{\rho_{\text{f}} U^2}, \ \mathbf{g}_{\text{s}}^* = \frac{\mathbf{g}_{\text{s}} L}{U^2}, \ m^* = \frac{\rho_{\text{s}}}{\rho_{\text{f}}},$$

are used to nondimensionalize Eq. (41) as follow

$$m^* \left( \ddot{\mathbf{d}} - \mathbf{g}_{\text{s}} \right) - \nabla \cdot \boldsymbol{\sigma}_{\text{s}} = \mathbf{0}, \tag{44}$$

where $m^*$ is the mass ratio. Eq. (44) is completed with incorporation of specified initial and boundary conditions.

### 4.2. Spatial discretization for the solid

Once the Galerkin approximation procedure is finished, we actually get the smoothed incremental equilibrium equation for dynamic analysis

$$\widetilde{\mathbf{K}}^n \Delta \bar{\mathbf{d}} = \widetilde{\mathbf{R}}^{n+1} - \widetilde{\mathbf{P}}^n - \mathbf{M}_{\text{s}} \ddot{\bar{\mathbf{d}}}^{n+1}, \tag{45}$$

where $\Delta \bar{\mathbf{d}} = \bar{\mathbf{d}}^{n+1} - \bar{\mathbf{d}}^n$ represents the increment of nodal displacement, $\widetilde{\mathbf{K}}$ denotes the smoothed tangent stiffness matrix, $\widetilde{\mathbf{R}}$ indicates the smoothed external force, $\widetilde{\mathbf{P}}$ is the smoothed internal force and $\mathbf{M}_{\text{s}}$ means the mass matrix. The linearization of Eq. (45) is implemented with recourse to the modified Newton–Raphson iterations considering the total Lagrangian scheme [56]. The reader may be referred to the early publications [2,48,57] for more technical details of the geometrically nonlinear analyses with the CS-FEM.

### 4.3. Time marching

The equation of structural motion is advanced in time with the generalized-$\alpha$ method which possesses controllable algorithmic dissipation in higher modes and minimizes adverse low-frequency dissipation [58]. The structural unknowns at the generalized midpoints can be analytically derived from

$$\ddot{\bar{\mathbf{d}}}^{n+1-\alpha_{\text{m}}} = \frac{1 - \alpha_{\text{m}}}{\beta (\Delta t)^2} (\bar{\mathbf{d}}^{n+1} - \bar{\mathbf{d}}^n) - \frac{1 - \alpha_{\text{m}}}{\beta \Delta t} \dot{\bar{\mathbf{d}}}^n - \frac{1 - \alpha_{\text{m}} - 2\beta}{2\beta} \ddot{\bar{\mathbf{d}}}^n, \tag{46}$$

$$\dot{\bar{\mathbf{d}}}^{n+1-\alpha_{\text{f}}} = \frac{(1 - \alpha_{\text{f}})\gamma}{\beta \Delta t} (\bar{\mathbf{d}}^{n+1} - \bar{\mathbf{d}}^n) - \frac{(1 - \alpha_{\text{f}})\gamma - \beta}{\beta} \dot{\bar{\mathbf{d}}}^n - \frac{(\gamma - 2\beta)(1 - \alpha_{\text{f}})}{2\beta} \Delta t \ddot{\bar{\mathbf{d}}}^n, \tag{47}$$

where the time integration parameters $\beta$, $\gamma$, $\alpha_{\text{m}}$ and $\alpha_{\text{f}}$ are determined by

$$\beta = \frac{1}{4}(1 - \alpha_{\text{m}} + \alpha_{\text{f}})^2, \ \gamma = \frac{1}{2} - \alpha_{\text{m}} + \alpha_{\text{f}}, \ \alpha_{\text{m}} = \frac{2\rho_\infty - 1}{\rho_\infty + 1}, \ \alpha_{\text{f}} = \frac{\rho_\infty}{\rho_\infty + 1}, \tag{48}$$

together with the spectral radius $\rho_\infty \in [0, \ 1]$ [58]. Furthermore, the smoothed internal force at the general midpoint is approximated in accordance with Kuhl and Crisfield [59].

## 5. Mesh deformation method

Without doubt, precisely capturing time-varying interfaces plays a vital part in VFSI simulations. In this paper, we present an efficient two-level mesh deformation method that marries the moving submesh approach (MSA) [60] with the ortho-semi-torsional spring analogy method (OST-SAM) [61]. The basic idea behind the MSA is to instantaneously update the fluid mesh over which a layer of very sparse submesh is placed for interpolation. The procedure of the present mesh moving technique is outlined as follow

Step 1: Extract the meshing information
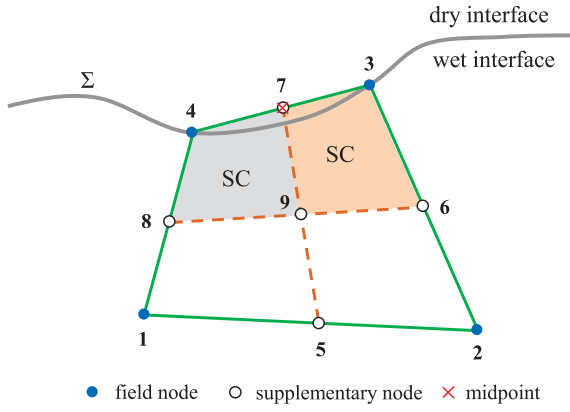Step 2: Collect all mesh nodes falling into each submesh zone

**Fig. 3.** Gradient smoothing for fluidic excitation along the interface.

Step 3: Compute interpolation functions of each mesh node
Step 4: Begin the time loop

    4.1: Gain displacements of boundary nodes of the solid
    4.2: Invoke the OST-SAM if interior submesh points appear
    4.3: Update the submesh
    4.4: Interpolate the mesh based on the new submesh
    4.5: Check the quality of the renewed mesh

Step 5: End the time loop

It is important to note that three-node triangular (T3) element is always feasible for the submesh due to its generality [60]. The quasi-static equilibrium equations of the OST-SAM are iteratively solved with the simple successive over-relaxation algorithm [62] since the coarse submesh results in a small-scale OST spring network. Technical details of the present two-level method are documented in our early paper [27]. Without the MSA, the OST-SAM will prove too costly for mesh updating [63].

## 6. Partitioned solution strategy

### 6.1. Interface coupling conditions

The permanent interplay between the viscoelastic fluid and the submerged elastic solid is realized by imposing the velocity continuity and stress equilibrium on the interface $\Sigma$

$$\mathbf{u} = \dot{\mathbf{d}} \quad \text{and} \quad \widetilde{\mathbf{t}}_\text{f} = \widetilde{\mathbf{t}}_\text{s}, \tag{49}$$

where $\widetilde{\mathbf{t}}_\text{f} = \widetilde{\boldsymbol{\sigma}}_\text{f} \cdot \mathbf{n}_{\Sigma_\text{s}}$ and $\widetilde{\mathbf{t}}_\text{s} = \widetilde{\boldsymbol{\sigma}}_\text{s} \cdot \mathbf{n}_{\Sigma_\text{s}}$ are the smoothed tractions of the fluid and solid, respectively, $\Sigma_\text{s}$ denotes the structural side of $\Sigma$ and $\mathbf{n}_{\Sigma_\text{s}}$ signifies the unit outward normal to $\Sigma_\text{s}$.

Here, the viscoelastic fluid traction passed on to the structure is evaluated in tandem with the unique cell-based gradient smoothing concept rather than the traditional Gaussian integration. As illustrated in Fig. 3, either of the two SCs in an interface element is certainly available for the fluidic excitation calculation. The applied fluid forces are thus determined by definition in the chosen SC

$$
\begin{aligned}
\widetilde{\mathbf{R}} &= \int_\Sigma \mathbf{N}^\text{T} \widetilde{\mathbf{t}}^\text{s} \, d\Gamma = \int_\Sigma \mathbf{N}^\text{T} \left( -p\mathbf{I} + \frac{2\eta}{Re}\widetilde{\boldsymbol{\epsilon}} + \frac{1-\eta}{ReWi}(\mathbf{c}-\mathbf{I}) \right) \mathbf{n}_{\Sigma_\text{s}} \, d\Gamma \\
&= \sum_{i=1}^{m_\text{fs}} \mathbf{N}^\text{T}(\mathbf{x}_i^\text{mp}) \left( -p(\mathbf{x}_i^\text{mp})\mathbf{I} + \frac{\eta}{Re}\left(\widetilde{\nabla}\mathbf{u}(\mathbf{x}_i^\text{mp}) + (\widetilde{\nabla}\mathbf{u}(\mathbf{x}_i^\text{mp}))^\text{T}\right) + \frac{1-\eta}{ReWi}(\mathbf{c}(\mathbf{x}_i^\text{mp}) - \mathbf{I}) \right) \\
&\quad \times \mathbf{n}_{\Sigma_\text{s}}(\mathbf{x}_i^\text{mp}) l_i,
\end{aligned}
\tag{50}
$$

where $\widetilde{\epsilon}$ is the smoothed deformation rate tensor and $m_\text{fs}$ defines the number of constituent segments of the interface.

### 6.2. Stabilized CBS(B)-based partitioned semi-implicit coupling algorithm

The formulated VFSI problem embraces a set of coupled nonlinear algebraic equations to be solved at each time step. The CBS scheme allows us to divide the coupled system into the explicit and implicit stages. At this point, the DEVSS-G/CBS(B)-SPGP stabilization is introduced to enhance the numerical stability of the CBS-based partitioned semi-implicit coupling algorithm [35]. To begin with, a second-order predictor [64] is adopted to predict the interface at the explicit phase. The velocity and pressure gradients and the conformation tensor are explicitly treated therein as well. The block Gauss–Seidel iterative procedure [65] is carried out for implicit coupling between the fluid projection and structural motion. The end-of-step velocity is included within the subiterations in the interest of the stability [36]. The main steps of the stabilized CBS(B)-based partitioned semi-implicit coupling algorithm are elaborated below

Step 1: Initialize all field variables and set the count $k = 0$
Step 2: Perform the explicit coupling step

    2.1: Extrapolate the position of the fluid–structure interface

$$\hat{\mathbf{x}}_\Sigma^{n+1(k)} = \mathbf{d}_\Sigma^n + \left(\frac{3}{2}\dot{\mathbf{d}}_\Sigma^n - \frac{1}{2}\dot{\mathbf{d}}_\Sigma^{n-1}\right)\Delta t,$$

    2.2: Move the fluid mesh $\Omega_\text{f}^{n+1(k)}$ using the two-level approach

    2.3: Assess the mesh velocity and other necessary geometric quantities

$$\mathbf{u}_\text{m}^{n+1(k)} = \frac{\mathbf{x}^{n+1(k)} - \mathbf{x}^n}{\Delta t},$$

    2.4: Calculate the two auxiliary variables

$$\mathbf{M}_\text{f}\bar{\mathbb{G}}^n = \widetilde{\mathbf{G}}\bar{\mathbf{u}}^n \quad \text{and} \quad \mathbf{M}_\text{f}\bar{\mathbf{q}}^n = \widetilde{\mathbf{G}}\bar{\mathbf{p}}^n,$$

    2.5: Predict the velocity

$$
\begin{aligned}
\mathbf{M}_\text{f}(\bar{\mathbf{u}}^{n+1(k)} - \bar{\mathbf{u}}^n) = &-\Delta t \left( \widetilde{\mathbf{C}}_\text{u}^n \bar{\mathbf{u}}^n + \widetilde{\mathbf{G}}\bar{\mathbf{p}}^n + \frac{\eta+\theta}{Re}\widetilde{\mathbf{H}}\bar{\mathbf{u}}^n + \frac{\theta}{Re}\widetilde{\mathbf{G}}\bar{\mathbb{G}}^n - \frac{1-\eta}{ReWi}\widetilde{\mathbf{G}}\bar{\mathbf{b}}^n \right) \\
&- \frac{(\Delta t)^2}{2} \left( \widetilde{\mathbf{K}}_\text{u}^n \bar{\mathbf{u}}^n + \widetilde{\mathbf{Q}}^n \bar{\mathbf{p}}^n + \frac{\theta}{Re}\widetilde{\mathbf{Q}}^n \bar{\mathbb{G}}^n - \frac{1-\eta}{ReWi}\widetilde{\mathbf{Q}}^n \bar{\mathbf{b}}^n \right),
\end{aligned}
$$

    2.6: Determine the conformation tensor

$$
\begin{aligned}
\mathbf{M}_\text{f}(\bar{\mathbf{c}}^{n+1(k)} - \bar{\mathbf{c}}^n) = &-\Delta t \left( \widetilde{\mathbf{C}}_\text{u}^n \bar{\mathbf{c}}^n - \widetilde{\mathbf{D}}_\text{c}^n \bar{\mathbf{c}}^n + \frac{1}{Wi}(\mathbf{M}_\text{f}\bar{\mathbf{c}}^n - \mathbf{I}) \right. \\
&\left. + \frac{\Delta t}{2} \left( \widetilde{\mathbf{K}}_\text{u}^n \bar{\mathbf{c}}^n - \widetilde{\mathbf{E}}_\text{c}^n \bar{\mathbf{c}}^n + \frac{1}{Wi}(\widetilde{\mathbf{L}}^n \bar{\mathbf{c}}^n - \mathbf{I}) \right) \right),
\end{aligned}
$$

Step 3: Perform the implicit coupling step

    3.1: Start fixed-point iterations and set $k \leftarrow k+1$
    3.2: Update the pressure

$$\widetilde{\mathbf{H}}\bar{\mathbf{p}}^{n+1(k)} = -\frac{1}{\Delta t + \phi} \left( \widetilde{\mathbf{G}}\bar{\mathbf{u}}^{n+1(k-1)} - \Delta t \widetilde{\mathbf{H}}\bar{\mathbf{p}}^n + \phi\widetilde{\mathbf{G}}\bar{\mathbf{q}}^n \right),$$

    3.3: Correct the velocity

$$\mathbf{M}_\text{f}(\bar{\mathbf{u}}^{n+1(k)} - \bar{\mathbf{u}}^{n+1(k-1)}) = -\Delta t \left( \widetilde{\mathbf{G}}(\bar{\mathbf{p}}^{n+1(k)} - \bar{\mathbf{p}}^n) + \frac{\Delta t}{2}\widetilde{\mathbf{Q}}^n(\bar{\mathbf{p}}^{n+1(k)} - \bar{\mathbf{p}}^n) \right),$$

    3.4: Evaluate the fluid force $\widetilde{\mathbf{R}}^{n+1(k)}$ and pass it on to the immersed solid
    3.5: Solve the elastodynamics equation by the Newton and generalized-$\alpha$ methods

$$
\begin{aligned}
\left( \frac{1-\alpha_\text{m}}{\beta(\Delta t)^2}\mathbf{M}_\text{s} + (1-\alpha_\text{f})\widetilde{\mathbf{K}}^{n+1(k)} \right) \bar{\mathbf{d}}^{n+1(k)} = &(1-\alpha_\text{f})\widetilde{\mathbf{R}}^{n+1(k)} + \alpha_\text{f}\widetilde{\mathbf{R}}^n - \alpha_\text{f}\widetilde{\mathbf{K}}^{n+1(k)}\bar{\mathbf{d}}^n + \\
&\mathbf{M}_\text{s}\left( \frac{1-\alpha_\text{m}}{\beta(\Delta t)^2}\bar{\mathbf{d}}^n + \frac{1-\alpha_\text{m}}{\beta\Delta t}\dot{\bar{\mathbf{d}}}^n + \frac{1-\alpha_\text{m}-2\beta}{2\beta}\ddot{\bar{\mathbf{d}}}^n \right),
\end{aligned}
$$

    3.6: Estimate the interfacial residuals

$$\mathbf{r}^{n+1(k)} = \mathbf{x}_\Sigma^{n+1(k)} - \hat{\mathbf{x}}_\Sigma^{n+1(k-1)},$$

**Table 1**
The meshing information of the cavity flow problem.

| Item | Fluid | | | Solid | | | Submesh | | |
|---|---|---|---|---|---|---|---|---|---|
| | M1 | M2 | M3 | M1 | M2 | M3 | M1 | M2 | M3 |
| Element type | Q4 | Q4 | Q4 | Q4 | Q4 | Q4 | T3 | T3 | T3 |
| Number of elements | $24 \times 24$ | $32 \times 32$ | $40 \times 40$ | $24 \times 1$ | $32 \times 1$ | $40 \times 1$ | 69 | 99 | 115 |
| Number of nodes | 625 | 1089 | 1681 | 50 | 82 | 122 | 50 | 69 | 82 |

3.7: Check the convergence: proceed to the next time step if convergent; otherwise go ahead

3.8: Relax the position of the interface

$$\hat{\mathbf{x}}_{\Sigma}^{n+1(k)} = \kappa \mathbf{x}_{\Sigma}^{n+1(k)} + (1-\kappa)\hat{\mathbf{x}}_{\Sigma}^{n+1(k-1)},$$

3.9: Compute the new mesh velocity on $\Sigma$

$$\mathbf{u}_{\mathrm{m}\Sigma}^{n+1(k)} = \frac{\hat{\mathbf{x}}_{\Sigma}^{n+1(k)} - \mathbf{x}_{\Sigma}^{n}}{\Delta t},$$

3.10: Return

A constant relaxation factor $\kappa$ is used for the above subiterative coupling process to which dynamic relaxations [12,66,67] may be preferably applied. In NFSI [36], the SPGP technique is helpful to reach extremely low mass ratios while preserving the second-order pressure accuracy. The positive impacts of the DEVSS-G/CBS(B)-SPGP stabilization on VFSI will be interpreted in the next section.

## 7. Numerical example

The numerical example is concerned with a leaky square cavity equipped with a flexible thin bottom. This benchmark problem is originally designed by Mok and Wall [68] for NFSI, currently serving as a popular example for testing various FSI solvers. Fig. 4 depicts the problem definition in reference to the undeformed configuration. An incompressible Oldroyd-B fluid gets into and comes out of the square cavity through small breaches near the top lid moving in the tangential direction. The elastic bottom fixed at two ends is excited to freely oscillate thanks to the motion of the viscoelastic fluid inside the cavity. The side length of the cavity is $L = 1$ and its elastic bottom is $b = 0.002$ thick. Both inlet and outlet are assumed to be 0.1 in length. A harmonically oscillating velocity with the angular frequency $\omega = \frac{2}{5}\pi$ is enforced along the top lid. The inflow and outflow conditions are identical to those in [69]: the inflow velocity $u_{\mathrm{in}}$ linearly varies from 0 to $u_1$ along the inlet while the pressure-free condition is applied at the outlet. No-slip condition is imposed on the two lateral rigid walls and the upper surface of the bottom. The physical parameters of the VFSI system are given as: $\rho_{\mathrm{f}} = 1$, $\mu = 0.01$, $\eta = 0.5$, $Wi = 0.1$, $Re = 100$, $\rho_{\mathrm{s}} = 500$, $E = 250$ and $\nu = 0$.

The mesh sensitivity is first investigated by varying the FE resolution. Three different meshes are utilized here to make sure consistent convergence of the developed method with mesh refinement. The generation of the FE mesh and MSA submesh is summarized in Table 1. The square cavity and thin membrane are uniformly discretized with Q4 elements. The schematic representation of M3 and its corresponding submesh is displayed in Fig. 5. Appropriate time step size is assigned to each mesh while zero-valued field variables are initiated at $t = 0$.

To quantitatively examine the mesh independence, Table 2 lists the vertical amplitude $A_2$, peak of vertical displacement $d_{2,\mathrm{max}}$, its mean value $d_{2,\mathrm{mean}}$ and root-mean-square error (RMSE) $d_{2,\mathrm{rmse}}$, and oscillation frequency $f_{\mathrm{o}}$ calculated on the three meshes. Note that the measuring point is placed in the middle of the top of the thin bottom. Generally speaking, the deviation among the three sets of computed parameters is negligible in the table. Moreover, all computed oscillation frequencies are equal and very close to the driving frequency $f = \frac{\omega}{2\pi} = 0.2$. In each case, the finite deformation of the flexible thin membrane has been successfully induced by the cavity flow which is driven by the periodic tangential velocity specified on the top lid. The time evolution of $d_2$ and

**Table 2**
Summary of some computed parameters on different meshes.

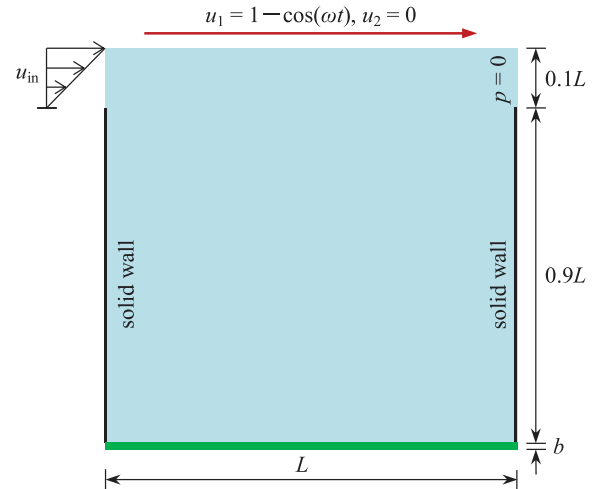| Mesh | $A_2$ | $d_{2,\mathrm{max}}$ | $d_{2,\mathrm{mean}}$ | $d_{2,\mathrm{rmse}}$ | $f_{\mathrm{o}}$ |
|---|---|---|---|---|---|
| M1 | 0.0272 | 0.318 | 0.2902 | 0.0161 | 0.205 |
| M2 | 0.0261 | 0.331 | 0.2980 | 0.0180 | 0.205 |
| M3 | 0.0264 | 0.320 | 0.2940 | 0.0172 | 0.205 |



**Fig. 4.** Viscoelastic fluid flow inside an open cavity with a flexible bottom.

$c$ at the measuring point are shown in Fig. 6, respectively. It is clearly observed from both pictures that all meshes engender almost the same time histories of the two selected variables. Different from [9,70], the inertia of the flexible solid brings about the positive mean displacement among all cases. The stable periodic oscillations are well established after a growth phase and the deflections away from the horizontal axis are relatively large. Based upon the above observation, M3 is employed for further analyses of the VFSI problem.

Fig. 7 compares the time histories of the measuring point using the developed semi-implicit method and the implicit approach presented in [2], respectively. It is revealed in the picture that the current method inspires somewhat higher-amplitude oscillations than the implicit coupling method does [2]. The evident deviation among different computer simulations also takes place in NFSI seeing that Habchi et al. [69] summarized some previous results from the open literature. We are not surprised by the difference as the open cavity flow itself is highly sensitive to boundary conditions as well as numerical approaches. Furthermore, the transition from the initialization phase to periodic phase happens at $t = 16.5$ which seems fairly close to the time slice given in [71]. In summary, the predicted vertical displacement curve is reasonable in this paper.

To highlight the stabilization effect of the presented semi-implicit coupling method, Fig. 8 monitors the time-dependent profiles of vertical displacement calculated with and without the DEVSS-G/CBS(B)-SPGP stabilizer. Both the CBS(A)-based and CBS(B)-based semi-implicit coupling algorithms proposed by He et al. [35,36] are deliberately run for comparison. Fig. 8 reveals that the first-order CBS(A)-based scheme fails to ensure correct flow-induced responses of the flexible bottom. The second-order CBS(B)-based scheme, even equipped with
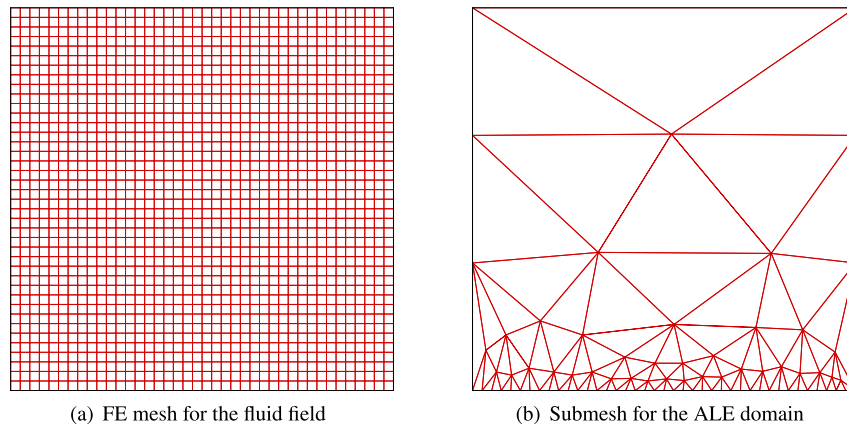
(a) FE mesh for the fluid field  (b) Submesh for the ALE domain

**Fig. 5.** Snapshots of medium mesh and submesh of the VFSI problem.



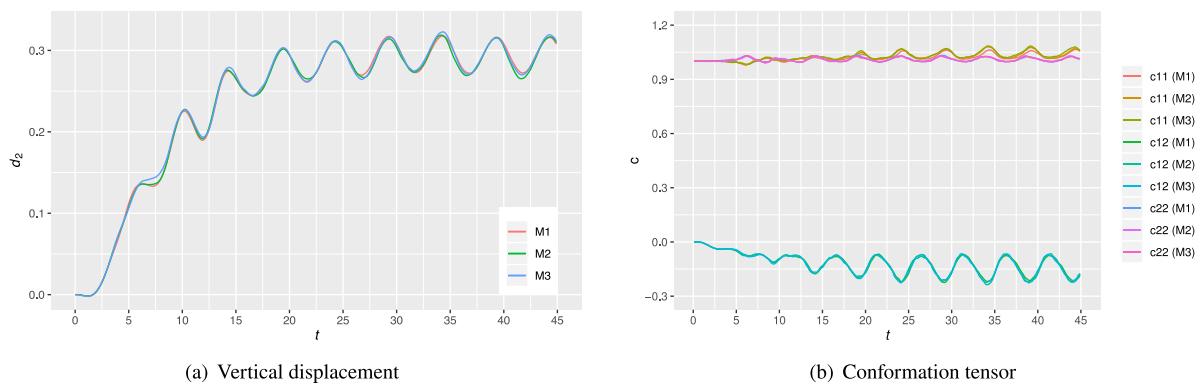(a) Vertical displacement  (b) Conformation tensor

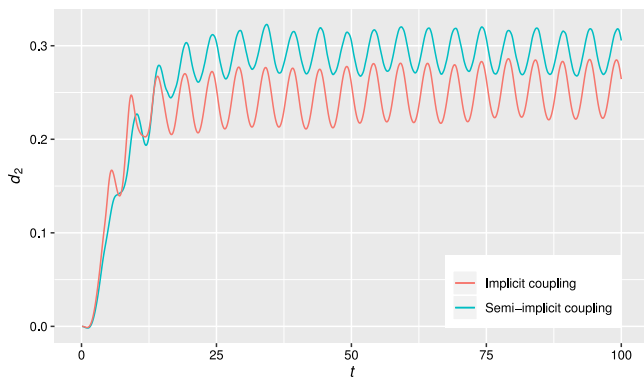**Fig. 6.** Time histories of the measuring point based on different meshes.



**Fig. 7.** Comparison of displacement evolution using semi-implicit and implicit coupling solvers.
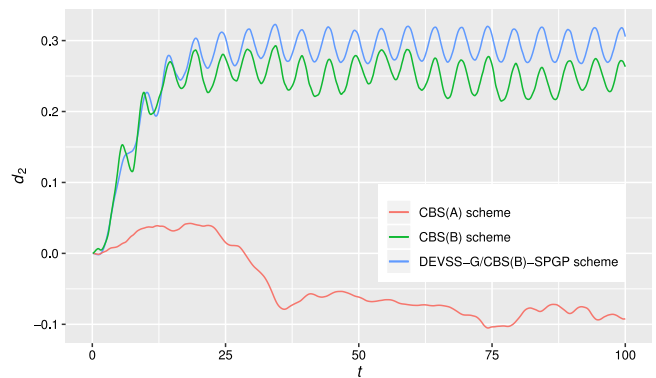


**Fig. 8.** Computation of vertical displacement with and without DEVSS-G/CBS(B)-SPGP stabilization.

the DEVSS-G technique, has also underperformed in this event since the exposed oscillations of the measuring point show some destabilizing characteristics. Xue et al. [72] explained that, for transient viscoelastic fluid flows with inertia force, the stabilizers aimed at steady-state situations may alter the equation type or overly diffuse the velocity field in the presence of solvent viscosity. It is thus realized that, the CBS-based partitioned semi-implicit coupling methods are very likely to predict inaccurate VFSI phenomena on condition that the DEVSS-G/CBS(B)-SPGP technique is not activated. In our numerical experiments, the CBS(B)-SPGP method is a good remedy to both the DEVSS-G formulation and second-order pressure splitting error such that the combined DEVSS-G/CBS(B)-SPGP stabilization has rendered a

valuable capability to considerably improve inferior numerical results in Fig. 8.

Referring to Huang et al. [73], we gradually change the structural density in an effort to further understand the stability of the presented semi-implicit coupling method. To be specific, $\rho_s = 100, 200, 400$ and 500 are calculated in Fig. 9 for plotting the evolution of $d_2$ and $p$, respectively. The structural density much smaller than those of [9,73] is reached here. We are aware that, in the analytical mass–spring–dashpot model [9], extensive implicit iterations are required at each time step for small solid-to-fluid mass ratio, indicating that numerical difficulties are probably encountered as a result of the added-mass effect [74]. Applying fixed-point iterations along with constant relaxation, the
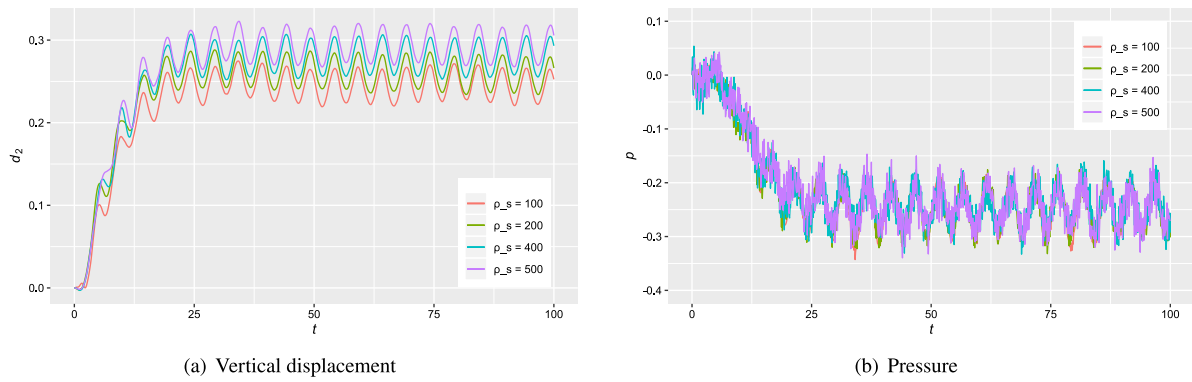
(a) Vertical displacement



(b) Pressure

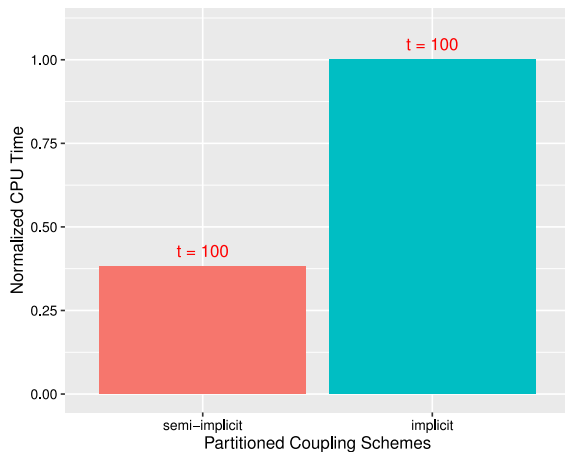**Fig. 9.** Time histories of the measuring point based on different structural densities.



**Fig. 10.** Efficiency comparison between the semi-implicit and implicit coupling schemes.

present study asks for just a few subiterations per time step between the fluid projection and structural motion. The proposed semi-implicit scheme demands far less subiterations per time step than previous implicit scheme [2]. Seen from Fig. 9, periodic vibrations and fluctuating pressure of the structure have been authentically established at various densities. Meanwhile, no spurious oscillations are reported at all among all cases. It is inferred that the presented method adapts to the adverse added-mass effect [74] better, as is the case of NFSI [36]. Fig. 9(a) reports a downward trend both in deflection and amplitude being calculated at diminished structural densities. This is because that the inertial force of the solid continuum becomes weaker with the decrease of the structural density and thus is easier to be counteracted by the viscoelastic fluid forces. The pressure appears less sensitive to the change in structural density in Fig. 9(b). The periodic steady-state evolution of $p$ is visibly exposed therein when $t > 25$. So far, the importance of preserving and stabilizing the second-order splitting error in pressure via the SPGP technique for the DEVSS-G formulation of the momentum equation has been attached to the CBS-based semi-implicit coupling algorithm in the VFSI analysis.

A comparative analysis of computational efficiency of the semi-implicit and implicit coupling schemes is provided in Fig. 10. The nondimensional time $t = 100$ is taken into account as this elapsed time is sufficient to stimulate a large number of stable periodic oscillations of the elastic structure. Seen from Fig. 10, the semi-implicit algorithm surprisingly makes a saving of over 60% computing expense over its implicit counterpart [2]. By contrast, the implicit algorithm is too costly at this time. Hence, the present stabilized semi-implicit coupling method manifests itself as a faster solution to VFSI.

The contours of the streamlines as well as the deflection of the solid at a few representative time instants are chronologically presented in Fig. 11. These streamlines demonstrate that the viscoelastic fluid flow is circulated throughout the cavity thanks to the moving top lid. Accordingly, the elastic bottom undergoes finite deformation and strong oscillations thanks to the internal circulation of the fluid flow. Since the Oldroyd-B fluid does not have the shear-thinning/shear-thickening property, the resultant flow phenomena seem rather similar to those of NFSI. For example, the vortices are identified at both left-lower and right-lower corners of the square domain. It is also observed that, the velocity layer parallel to the moving lid becomes significantly thinner when the periodic oscillations are fully established. Thus it is easy to recognize that the predicted streamlines coincide with, to a large extent, not only the contours of VFSI [40,43] but also the composite illustration in NFSI [69,73,75].

## 8. Conclusions

In this contribution, the DEVSS-G/CBS(B)-SPGP stabilization has been proposed for the CBS-based partitioned semi-implicit coupling algorithm with application to transient VFSI analysis. The constitutive equation of the Oldroyd-B fluid is expressed in terms of the conformation tensor to strengthen the positive definiteness since the DEVSS-G algorithm is general. The combined NS and constitutive equations are resolved with the help of the DEVSS-G/CBS(B)-SPGP stabilizer such that the second-order pressure accuracy is still retained in the fractional-step procedure. The elastodynamics equation of the geometrically nonlinear solid is linearized through the modified Newton–Raphson procedure incorporating the generalized-$\alpha$ time marching method. The entire VFSI system is formulated in the ALE-CS-FEM notion where all gradient related terms are smoothed for the softening effect. Particularly, the cell-based smoothing gradient concept is used for imposition of the viscoelastic traction along the deformable interface. The partitioned semi-implicit coupling algorithm makes use of the second-order CBS(B) scheme to form the explicit–implicit coupling of fluid and solid media by splitting the NS equations into two main stages. Here, the end-of-step velocity is compulsorily iterated at the implicit stage. The established framework can gain computational benefits from both the CBS(B) fluid solver and the modified semi-implicit coupling procedure. The DEVSS-G/CBS(B)-SPGP formulation that perfectly conforms to such a staggered solution provides very good stabilization for the semi-implicit VFSI coupling. It is seen that the simple block-Gauss–Seidel produce shows excellent performance during the implicit subiterations per time step even without invoking any accelerator. A well-known VFSI model problem is subsequently analyzed in detail using the proposed methodology. The major features of mixed viscoelastic flow and flow-induced vibration are successfully captured. The comparison with existing numerical algorithms has emphasized the advantages of the developed semi-implicit coupling scheme. In this event, we are impressed
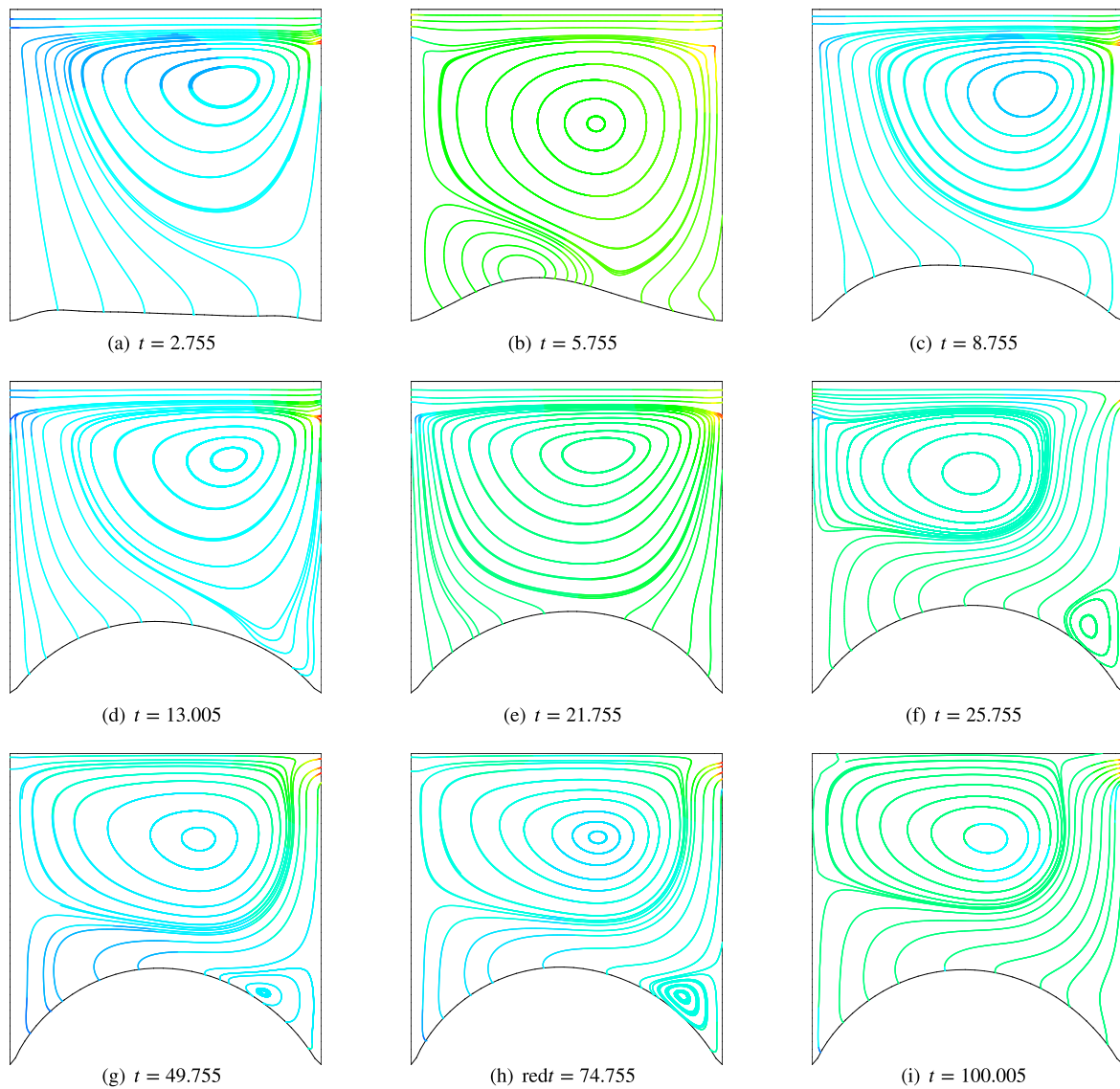
(a) $t = 2.755$    (b) $t = 5.755$    (c) $t = 8.755$

(d) $t = 13.005$    (e) $t = 21.755$    (f) $t = 25.755$

(g) $t = 49.755$    (h) red$t = 74.755$    (i) $t = 100.005$

**Fig. 11.** Snapshots of the streamlines and deflection of the bottom at various time slices.

by the DEVSS-G/CBS(B)-SPGP stabilization with which the CBS-based partitioned semi-implicit coupling algorithm is capable of improving the stability considerably and boosting the efficiency dramatically.

**Declaration of competing interest**

The authors declare that they have no known competing financial interests or personal relationships that could have appeared to influence the work reported in this paper.

**References**

[1] A.A. Dey, Y. Modarres-Sadeghi, J.P. Rothstein, Observation of lock-in for viscoelastic fluid–structure interactions, J. Fluids Struct. 96 (2020) 103025.
[2] T. He, A strongly-coupled cell-based smoothed finite element solver for unsteady viscoelastic fluid–structure interaction, Comput. Struct. 235 (2020) 106264.
[3] K. Walters, M.F. Webster, The distinctive CFD challenges of computational rheology, Internat. J. Numer. Methods Fluids 43 (5) (2003) 577–596.
[4] D. Chakraborty, M. Bajaj, L. Yeo, J. Friend, M. Pasquali, J.R. Prakash, Viscoelastic flow in a two-dimensional collapsible channel, J. Non-Newtonian Fluid Mech. 165 (19–20) (2010) 1204–1218.
[5] D. Chakraborty, J.R. Prakash, Influence of shear thinning on viscoelastic fluid–structure interaction in a two-dimensional collapsible channel, Ind. Eng. Chem. Res. 50 (23) (2011) 13161–13168.
[6] K.-J. Bathe, Finite Element Procedures, Prentice-Hall, Inc., Upper Saddle River, New Jersey, USA, 1996.
[7] A.N. Brooks, T.J.R. Hughes, Streamline upwind/Petrov–Galerkin formulations for convection dominated flows with particular emphasis on the incompressible Navier–Stokes equations, Comput. Methods Appl. Mech. Engrg. 32 (1–3) (1982) 199–259.
[8] D. Chakraborty, J.R. Prakash, Viscoelastic fluid flow in a 2D channel bounded above by a deformable finite-thickness elastic wall, J. Non-Newtonian Fluid Mech. 218 (2015) 83–98.
[9] X. Chen, M. Schäfer, D. Bothe, Numerical modeling and investigation of viscoelastic fluid–structure interaction applying an implicit partitioned coupling algorithm, J. Fluids Struct. 54 (2015) 390–421.
[10] C.W. Hirt, A.A. Amsden, J.L. Cook, An arbitrary Lagrangian–Eulerian computing method for all flow speeds, J. Comput. Phys. 14 (3) (1974) 227–253.
[11] J.G. Oldroyd, On the formulation of rheological equations of state, Proc. R. Soc. Lond. Ser. A Math. Phys. Eng. Sci. 200 (1063) (1950) 523–541.
[12] U. Küttler, W.A. Wall, Fixed-point fluid–structure interaction solvers with dynamic relaxation, Comput. Mech. 43 (1) (2008) 61–72.

[13] M.M. Joosten, W.G. Dettmer, D. Perić, Analysis of the block Gauss–Seidel solution procedure for a strongly coupled model problem with reference to fluid–structure interaction, Int. J. Numer. Methods Eng. 78 (7) (2009) 757–778.

[14] A. Amini, A.S. Eghtesad, K. Sadeghy, Creeping flow of Herschel–Bulkley fluids in collapsible channels: A numerical study, Korea-Aust Rheol. J. 28 (4) (2016) 255–265.

[15] A. Amani, A. Naseri, C.D. Pérez-Segarra, A. Oliva, A method for fluid–structure interaction problems with non-Newtonian fluid, in: Proceedings of the 6th European Conference on Computational Mechanics (Solids, Structures and Coupled Problems) and the 7th European Conference on Computational Fluid Dynamics, Glasgow, UK, 2018, pp. 101–110.

[16] M.A. Fernández, J.F. Gerbeau, C. Grandmont, A projection semi-implicit scheme for the coupling of an elastic structure with an incompressible fluid, Int. J. Numer. Methods Eng. 69 (4) (2007) 794–821.

[17] H. Lee, S. Xu, Numerical approximation of viscoelastic fluid–structure interaction problems, Int. J. Numer. Anal. Mod. 15 (4–5) (2018) 579–593.

[18] Y. Xiong, S. Peng, M. Zhang, D. Yang, Numerical study on the vortex-induced vibration of a circular cylinder in viscoelastic fluids, J. Non-Newtonian Fluid Mech. 272 (2019) 104170.

[19] L. Zhu, An IB method for non-Newtonian-fluid flexible-structure interactions in three-dimensions, Comput. Model Eng. Sci. 119 (1) (2019) 125–143.

[20] G.R. Liu, K.Y. Dai, T.T. Nguyen, A smoothed finite element method for mechanics problems, Comput. Mech. 39 (6) (2007) 859–877.

[21] J. Étienne, E.J. Hinch, J. Li, A Lagrangian–Eulerian approach for the numerical simulation of free-surface flow of a viscoelastic material, J. Non-Newtonian Fluid Mech. 136 (2–3) (2006) 157–166.

[22] J. Hron, K.R. Rajagopal, K. Tůma, Flow of a Burgers fluid due to time varying loads on deforming boundaries, J. Non-Newtonian Fluid Mech. 210 (2014) 66–77.

[23] K. Tůma, J. Stein, V. Průša, E. Friedmann, Motion of the vitreous humour in a deforming eye–fluid-structure interaction between a nonlinear elastic solid and viscoelastic fluid, Appl. Math. Comput. 335 (2018) 50–64.

[24] C.A. Felippa, K.-C. Park, C. Farhat, Partitioned analysis of coupled mechanical systems, Comput. Methods Appl. Mech. Engrg. 190 (24–25) (2001) 3247–3270.

[25] C. Farhat, M. Lesoinne, Two efficient staggered algorithms for the serial and parallel solution of three-dimensional nonlinear transient aeroelastic problems, Comput. Methods Appl. Mech. Engrg. 182 (3) (2000) 499–515.

[26] P. Le Tallec, J. Mouro, Fluid structure interaction with large structural displacements, Comput. Methods Appl. Mech. Engrg. 190 (24) (2001) 3039–3067.

[27] T. He, K. Zhang, An overview of the combined interface boundary condition method for fluid–structure interaction, Arch. Comput. Methods Eng. 24 (4) (2017) 891–934.

[28] A.J. Chorin, Numerical solution of the Navier–Stokes equations, Math. Comput. 22 (104) (1968) 745–762.

[29] R. Témam, Une méthode d'approximation de la solution des équations de Navier–Stokes, Bull. Soc. Math. France 96 (1968) 115–152.

[30] M. Astorino, F. Chouly, M.A. Fernández, Robin based semi-implicit coupling in fluid–structure interaction: stability analysis and numerics, SIAM J. Sci. Comput. 31 (6) (2009) 4041–4065.

[31] F. Nobile, M. Pozzoli, C. Vergara, Inexact accurate partitioned algorithms for fluid–structure interaction problems with finite elasticity in haemodynamics, J. Comput. Phys. 273 (2014) 598–617.

[32] A. Naseri, I. Gonzalez, A. Amani, C.D. Pérez-Segarra, A. Oliva, A second-order time accurate semi-implicit method for fluid–structure interaction problems, J. Fluids Struct. 86 (2019) 135–155.

[33] M.A. Fernández, F.M. Gerosa, An unfitted mesh semi-implicit coupling scheme for fluid-structure interaction with immersed solids, Int. J. Numer. Methods Eng. (2020) 1–25, http://dx.doi.org/10.1002/nme.6449.

[34] O.C. Zienkiewicz, P. Nithiarasu, R. Codina, M. Vazquez, P. Ortiz, The characteristic-based-split procedure: An efficient and accurate algorithm for fluid problems, Internat. J. Numer. Methods Fluids 31 (1) (1999) 359–392.

[35] T. He, A CBS-based partitioned semi-implicit coupling algorithm for fluid–structure interaction using MCIBC method, Comput. Methods Appl. Mech. Engrg. 298 (2016) 252–278.

[36] T. He, J. Yang, C. Baniotopoulos, Improving the CBS-based partitioned semi-implicit coupling algorithm for fluid–structure interaction, Internat. J. Numer. Methods Fluids 87 (9) (2018) 463–486.

[37] O.C. Zienkiewicz, R.L. Taylor, P. Nithiarasu, The Finite Element Method for Fluid Dynamics, Vol. 3, seventh ed., Butterworth-Heinemann, Oxford, UK, 2014.

[38] R. Codina, Pressure stability in fractional step finite element methods for incompressible flows, J. Comput. Phys. 170 (1) (2001) 112–140.

[39] P. Nithiarasu, O.C. Zienkiewicz, Analysis of an explicit and matrix free fractional step method for incompressible flows, Comput. Methods Appl. Mech. Engrg. 195 (41) (2006) 5537–5551.

[40] A. Amani, Numerical Simulation of non-Newtonian Fluid–Structure Interaction Problems (Master's thesis), Universitat Politècnica de Catalunya, 2018.

[41] T. He, A cell-based smoothed CBS finite element formulation for computing the Oldroyd-B fluid flow, J. Non-Newtonian Fluid Mech. 272 (2019) 104162.

[42] T. He, Insight into the cell-based smoothed finite element method for convection-dominated flows, Comput. Struct. 212 (2019) 215–224.

[43] T. He, A truly mesh-distortion-enabled implementation of cell-based smoothed finite element method for incompressible fluid flows with fixed and moving boundaries, Int. J. Numer. Methods Eng. 121 (14) (2020) 3227–3248.

[44] T. He, An efficient selective cell-based smoothed finite element approach to fluid–structure interaction, Phys. Fluids 32 (6) (2020) 067102.

[45] J.W. Yoo, B. Moran, J.S. Chen, Stabilized conforming nodal integration in the natural-element method, Int. J. Numer. Methods Eng. 60 (5) (2004) 861–890.

[46] J.S. Chen, C.T. Wu, S. Yoon, Y. You, A stabilized conforming nodal integration for Galerkin mesh-free methods, Int. J. Numer. Methods Eng. 50 (2) (2001) 435–466.

[47] G.R. Liu, T.T. Nguyen, Smoothed Finite Element Methods, CRC Press, Boca Raton, Florida, USA, 2010.

[48] K.Y. Dai, G.R. Liu, Free and forced vibration analysis using the smoothed finite element method (SFEM), J. Sound Vib. 301 (3) (2007) 803–820.

[49] M.A. Hulsen, A sufficient condition for a positive definite configuration tensor in differential models, J. Non-Newtonian Fluid Mech. 38 (1) (1990) 93–100.

[50] F.P.T. Baaijens, Mixed finite element methods for viscoelastic flow analysis: a review, J. Non-Newtonian Fluid Mech. 79 (2–3) (1998) 361–385.

[51] F.P.T. Baaijens, S.H.A. Selen, H.P.W. Baaijens, G.W.M. Peters, E.H.M. Han, Viscoelastic flow past a confined cylinder of a low density polyethylene melt, J. Non-Newtonian Fluid Mech. 68 (2) (1997) 173–203.

[52] R. Guénette, M. Fortin, A new mixed finite element method for computing viscoelastic flows, J. Non-Newtonian Fluid Mech. 60 (1) (1995) 27–52.

[53] Y. Bao, D. Zhou, C. Huang, Numerical simulation of flow over three circular cylinders in equilateral arrangements at low Reynolds number by a second-order characteristic-based split finite element method, Comput. Fluids 39 (5) (2010) 882–899.

[54] T. He, H. Zhang, K. Zhang, A smoothed finite element approach for computational fluid dynamics: applications to incompressible flows and fluid–structure interaction, Comput. Mech. 62 (5) (2018) 1037–1057.

[55] P. Nithiarasu, A fully explicit characteristic based split (CBS) scheme for viscoelastic flow calculations, Int. J. Numer. Methods Eng. 60 (5) (2004) 949–978.

[56] K.J. Bathe, E. Ramm, E.L. Wilson, Finite element formulations for large deformation dynamic analysis, Int. J. Numer. Methods Eng. 9 (2) (1975) 353–386.

[57] X.Y. Cui, G.R. Liu, G.Y. Li, X. Zhao, T.T. Nguyen, G.Y. Sun, A smoothed finite element method (SFEM) for linear and geometrically nonlinear analysis of plates and shells, Comput. Model Eng. Sci. 28 (2) (2008) 109–126.

[58] J. Chung, G.M. Hulbert, A time integration algorithm for structural dynamics with improved numerical dissipation: the generalized-α method, J. Appl. Mech.–Trans. ASME 60 (2) (1993) 371–375.

[59] D. Kuhl, M.A. Crisfield, Energy-conserving and decaying algorithms in non-linear structural dynamics, Int. J. Numer. Methods Eng. 45 (5) (1999) 569–599.

[60] E. Lefrançois, A simple mesh deformation technique for fluid–structure interaction based on a submesh approach, Int. J. Numer. Methods Eng. 75 (9) (2008) 1085–1101.

[61] G.A. Markou, Z.S. Mouroutis, D.C. Charmpis, M. Papadrakakis, The ortho-semi-torsional (OST) spring analogy method for 3D mesh moving boundary problems, Comput. Methods Appl. Mech. Engrg. 196 (4) (2007) 747–765.

[62] D. Zeng, C.R. Ethier, A semi-torsional spring analogy model for updating unstructured meshes in 3D moving domains, Finite Elem. Anal. Des. 41 (11) (2005) 1118–1139.

[63] T. He, T. Wang, H. Zhang, The use of artificial compressibility to improve partitioned semi-implicit FSI coupling within the classical Chorin–Témam projection framework, Comput. Fluids 166 (2018) 64–77.

[64] S. Piperno, Explicit/implicit fluid/structure staggered procedures with a structural predictor and fluid subcycling for 2D inviscid aeroelastic simulations, Internat. J. Numer. Methods Fluids 25 (10) (1997) 1207–1226.

[65] M. Cervera, R. Codina, M. Galindo, On the computational efficiency and implementation of block-iterative algorithms for nonlinear coupled problems, Eng. Comput. 13 (6) (1996) 4–30.

[66] T. Yamada, S. Yoshimura, Line search partitioned approach for fluid–structure interaction analysis of flapping wing, Comput. Model Eng. Sci. 24 (1) (2008) 51–60.

[67] J. Degroote, R. Haelterman, S. Annerel, P. Bruggeman, J. Vierendeels, Performance of partitioned procedures in fluid–structure interaction, Comput. Struct. 88 (7–8) (2010) 446–457.

[68] D.P. Mok, W.A. Wall, Partitioned analysis schemes for the transient interaction of incompressible flows and nonlinear flexible structures, in: W.A. Wall, K.-U. Bletzinger, K. Schweizerhof (Eds.), Trends in Computational Structural Mechanics, Barcelona, Spain, 2001, pp. 689–698.

[69] C. Habchi, S. Russeil, D. Bougeard, J.L. Harion, T. Lemenand, A. Ghanem, D.D. Valle, H. Peerhossaini, Partitioned solver for strongly coupled fluid–structure interaction, Comput. Fluids 71 (2013) 306–319.

[70] K.-J. Bathe, H. Zhang, A mesh adaptivity procedure for CFD and fluid–structure interactions, Comput. Struct. 87 (11–12) (2009) 604–617.

[71] A. Apostolatos, G. De Nayer, K.-U. Bletzinger, M. Breuer, R. Wüchner, Systematic evaluation of the interface description for fluid–structure interaction simulations using the isogeometric mortar-based mapping, J. Fluids Struct. 86 (2019) 368–399.

[72] S.-C. Xue, R.I. Tanner, N. Phan-Thien, Numerical modelling of transient viscoelastic flows, J. Non-Newtonian Fluid Mech. 123 (1) (2004) 33–58.

[73] D.Z. Huang, W. Pazner, P.-O. Persson, M.J. Zahr, High-order partitioned spectral deferred correction solvers for multiphysics problems, J. Comput. Phys. 412 (2020) 109441.

[74] P. Causin, J.-F. Gerbeau, F. Nobile, Added-mass effect in the design of partitioned algorithms for fluid–structure problems, Comput. Methods Appl. Mech. Engrg. 194 (42) (2005) 4506–4527.

[75] C. Kassiotis, A. Ibrahimbegovic, R. Niekamp, H.G. Matthies, Nonlinear fluid–structure interaction problem. Part I: implicit partitioned algorithm, nonlinear stability proof and validation examples, Comput. Mech. 47 (3) (2011) 305–323.